Journal of Applied Physics

Crystallographic analysis of nano-tendril bundle vs fuzz growth on tungsten exposed to helicon wave-coupled helium plasma

Cite as: J. Appl. Phys. **129**, 115301 (2021); https://doi.org/10.1063/5.0027438
Submitted: 28 August 2020 • Accepted: 08 February 2021 • Published Online: 15 March 2021

K. B. Woller, D. G. Whyte and G. M. Wright

Journal of Applied Physics ARTICLE scitation.org/journal/jap

Crystallographic analysis of nano-tendril bundle vs fuzz growth on tungsten exposed to helicon wave-coupled helium plasma

Cite as: J. Appl. Phys. **129**, 115301 (2021); doi: 10.1063/5.0027438
Submitted: 28 August 2020 · Accepted: 8 February 2021 ·
Published Online: 15 March 2021

K. B. Woller,[a] D. G. Whyte, and G. M. Wright

AFFILIATIONS

Plasma Science and Fusion Center, Massachusetts Institute of Technology, Cambridge, Massachusetts 02139, USA

[a]**Author to whom correspondence should be addressed:** kbwoller@mit.edu

ABSTRACT

The propensity for nano-tendril bundle (NTB) vs widespread nano-tendril growth (i.e., fuzz) on polycrystalline W under varying ion energy modulation conditions, from DC to peak-to-peak energy modulation of 42 eV at 13.56 MHz, is correlated with the crystal orientation of the underlying grains. Grains that are vicinal to crystal orientations with high surface diffusivity (e.g., {101} for a body centered cubic crystal structure) exhibit NTB growth at lower ion energy modulation amplitude than grains that are vicinal to low surface diffusivity orientations, such as {100}. Adatom mobility considerations are presented to describe the experimental observations. These results support that surface diffusion or W adatom mobility enhanced by ion bombardment plays a key role in the surface morphology evolution of W under He irradiation.

I. INTRODUCTION

Tungsten (W) nano-tendril morphology, also called W fuzz, is a spontaneous development of topographically complex surface structures under low-energy helium (He) ion bombardment. Tungsten fuzz is of general scientific interest in material and plasma–material interaction science, but also has potentially deleterious effects on the use of W in fusion energy devices where He ash can strike the exhaust surfaces. For example, the nano-tendrils of the W fuzz surface could be a source of dust and/or shortened component lifetime due to enhanced material removal and generally change the response of the W surface to the plasma.[1] Even as growth mechanisms continue to be studied, predictions of fuzz growth in ITER, for example, are accomplished through empirical analysis in a parameter space mostly dictated by surface temperature and ion energy.[2] There is general interest in W fuzz for other applications outside of fusion energy, as well. The modified surface layer dramatically changes the material properties of the surface, such as the emissivity and thermal diffusivity,[3] in a somewhat tunable fashion. The highly porous surface becomes optically black, making the surface an almost ideal blackbody absorber that could be utilized for thermo-photovoltaic collectors or as a beam dump in laser applications, if the surface temperature does not rise high to remediate the structures through annealing. Also, the nanoporous structure has been used in photocatalytic experiments to assess the performance of porous tungsten oxide for solar water-splitting.[4]

Researchers are also driven to understand why and how W fuzz forms, as fuzz growth has been observed on various metals.[5–7] Here, we define a nano-tendril as a protrusion of metal with typical width ∼10–50 nm and aspect ratio, length/width $\gg 1$, while fuzz is a uniform distribution of nano-tendrils across some surface area such that the original surface is covered by the tendrils and the surface becomes optically black, yet metallic. All physical models of W fuzz growth posit that the near-surface He bubble formation is the first step toward fuzz growth; these bubbles agglomerate within the first tens of nanometers of the surface due to insolubility of He in material.[8–16] After the initial setup, there are different pathways for nano-tendril growth to take, depending on the model. In some models, it is proposed that the He bubbles reach pressures that exceed the yield strength of W, inducing dislocation loop-punching in the bulk or causing bubbles at the surface to rupture, leaving thin pieces of the bubble shell behind as nucleation sites for the process to continue.[14–17] In other models, He bubbles with pressures marginally below that needed to overcome the yield strength

of W could lower the viscosity of the W on the surface and allow viscoelastic flow along the surface to deformities and nano-tendril tips.[18] Finally, there is the possibility that the He bubbles are a source of tensile stress in the surface, which lowers the chemical potential over the surface of bubbles, causing a net flux of adatoms generated by the He ion bombardment toward the bubble apexes, where the adatoms may become trapped and form the tendrils.[19,20] Previous measurements of the He concentration in the bubbles during the evolution of the surface show that He atom concentration in the surface is too low to represent He bubbles with $\sim 10^9$ Pa pressure necessary to overcome the yield strength of W.[21] Also, there is no obvious dependence of the He content in the surface of tungsten when exposed with various flux, fluence, and surface temperatures from different laboratories.[22] Thus, while He bubbles are present in the surface, they appear to be a necessary but insufficient requirement to produce W fuzz.

The recently discovered nano-tendril bundle (NTB) growth on W surfaces exposed to radiofrequency He plasma expanded the evolutionary tree of structures that form on W surfaces saturated with He.[23] It has been shown that NTB growth can be more rapid than W fuzz growth and may show another path for erosion of W surfaces in fusion devices.[24] Tungsten NTB growth, therefore, should also be considered when evaluating plasma-facing component operation in future fusion energy devices. Observations on the variety of W nanostructures have shown that W deposition from sacrificial W anode plasma seeding,[25] W redeposition or enhanced surface mobility from impurity seeding,[26] and surface buckling under non-uniform lateral compression[27] can all contribute to the structures that finally form on the surface.

We present new experimental observations that strongly support that He ion bombardment contributes to W adatom (a loosely bound surface atom) diffusion, which serves as the basis for the development of nanostructures that develop into some final nano-tendril form in low erosion He plasma conditions. With time modulated incident He ion energy, and manipulation of the surface defect kinetics, a diverse set of nanostructures develop simultaneously, which clearly reveal that surface kinetics govern the formation of the tendrils when supplied with mobile W atoms. Under a gradient in exposure conditions, different structures including corrugations, isolated nano-tendrils, nano-tendril bundles (NTBs), and fuzz (Fig. 1) develop. Each type of nanostructure provides information pertaining to the nature of the surface morphology changes.

II. METHODS

A. Material preparation

The samples were disks of 99.95% PLANSEE W with dimensions of 1 mm thickness and 25 mm diameter. The W disks were mechanically polished to a mirror finish. For clear orientation measurements, the W disks were electropolished using a 4% sodium hydroxide (NaOH) solution that was maintained at 0 °C in a stainless steel vessel, which served as the cathode for the electropolish circuit. The W disks were mounted in a polytetrafluoroethylene (PTFE) block with a voltage feedthrough such that only the polished side of the disk was exposed to the NaOH solution. A seal around the edge of the W disk within the PTFE block was created by coating the inside of the block with silicone grease. The PTFE block with the W disk mounted on it was placed in the NaOH solution, and the best electropolish conditions were found with a bias of 7 V and a current of 0.7 A, resulting in a current density of 0.2 A cm^{-2}. The current density was maintained for 45 s. Then, the PTFE block and disk were removed from the NaOH solution, rinsed in distilled water, rinsed in ethanol, and then air blown dry. The electropolished samples were kept in a container with silica gel desiccant to avoid oxidation as the samples were transported to the microscopy lab for orientation measurements.

B. Plasma exposure

The helicon plasma source of the Dynamics of ION Implantation and Sputtering Of Surfaces (DIONISOS) experiment[28] was the source of He ions. The experimental facility has a plasma excited by a Nagoya Type III antenna and confined by four water-cooled, copper Helmholtz coils, as shown in Fig. 2(a). The target is located ~0.40 m from the end of the antenna. The different characteristic modes of the 13.56 MHz RF plasma source affect the ion energy distribution incident on the samples.[29] In the inductively coupled mode, the plasma potential is approximately uniform. A sample that is placed in this plasma experiences an ion flux that has a narrow ion energy distribution, subjecting the sample to constant ion energy to within ±4 eV. A bias tee was fabricated that would allow a high frequency (13.56 MHz) potential modulation to be applied to the sample simultaneously with the DC bias. The resulting potential waveforms at the sample and on the atmospheric side of the bias feedthrough were checked with a high frequency probe at atmospheric pressure. It was found that there were minimal losses through the transmission line to the sample. The high frequency probe attached to the feedthrough was then used to monitor the sample potential waveform during plasma exposure.

The ion energy distribution was measured by a grid-collector retarding field analyzer[30] created by attaching the DC + RF transmission line to a grid mounted over a W sample. The grid wire spacing of such an analyzer has to be fine enough to prevent the ingress of plasma into the analyzer. The grid used in this analyzer had previously been designed and operated on the reciprocating retarding field energy analyzer of Alcator C-Mod,[31] with a grid wire spacing of 40 μm. The minimum Debye length of the highest density plasmas studied here in DIONISOS was 14 μm, just within the acceptable range for the spacing of the grid wires, which should be 2–4 Debye lengths at maximum.[32] The grid allowed an area of 1×1 mm^2 of the plasma to be tested with the rest of the area blocked by the grid holding plate. The grid plate could be positioned to allow for measurements at different radial locations. A schematic of this grid-collector energy analyzer is shown in Fig. 2(b) with a photo taken from the point of view of the plasma shown in Fig. 2(c). The grid and W disk were electrically isolated from each other. In this way, potential modulations could be applied to the grid while a potential ramp could be applied to the W disk. The derivative of the current collected on the W sample gives a measure of the ion energy distribution passing through the grid. The potential ramp was at a low frequency ($f_{ramp} = 0.8$ Hz) such that the measured current intensity is a measure of the time-averaged ion energy distribution. The measured current intensity

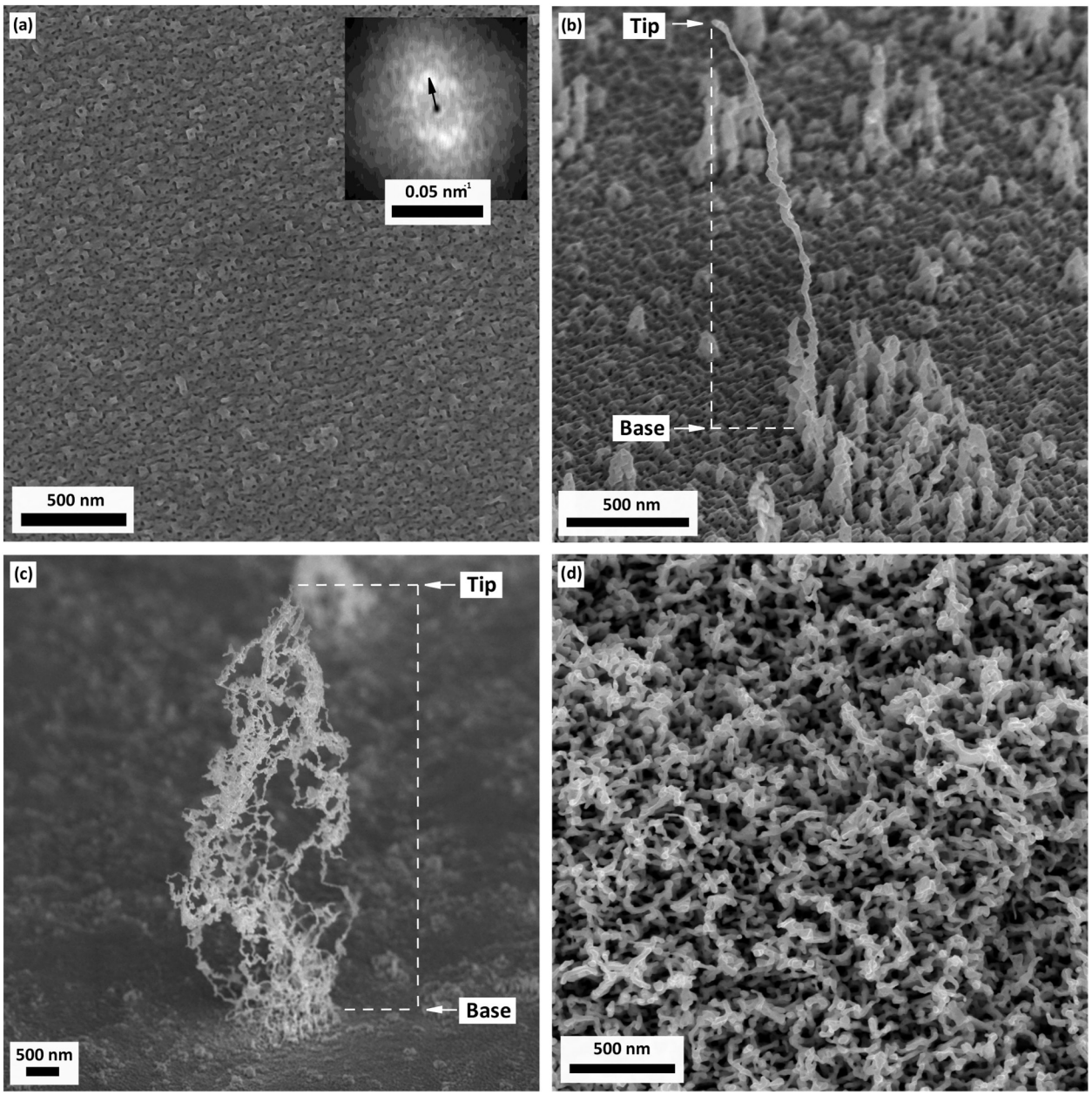

FIG. 1. (a) Surface corrugations with the characteristic wave number vector as represented by the 2D fast Fourier transform (FFT) in the inset image. (b) Isolated nano-tendril with nano-tendril nuclei at the base. (c) Nano-tendril bundle (NTB) growing normal to the surface. The corrugations (a), isolated nano-tendril (b), and NTB (c) were observed on the same sample, on separate grains. (d) Quasi-uniform fuzz layer. The growth conditions for the layer of fuzz are identical to (a), (b), and (c) but with a constant ion energy, i.e., with no applied energy modulation. Images (a) and (d) were taken with the imaging electron beam normal to the surface, while images (b) and (c) were taken with the sample normal tilted 52° from the electron beam axis to show normal structure.

by this analyzer is shown for a DC and a DC + RF bias applied to the grid in Fig. 3(b), for which self-biasing was measured to be negligible. Since the RF bias power supply was synchronized with the RF antenna power supply, the time-averaged ion energy distributions measured with the grid-collector retarding field analyzer are assumed to hold when the analyzer is replaced with the sample.

In the helicon wave-coupled mode, the plasma source antenna couples to the helicon wave in the plasma close to the RF power

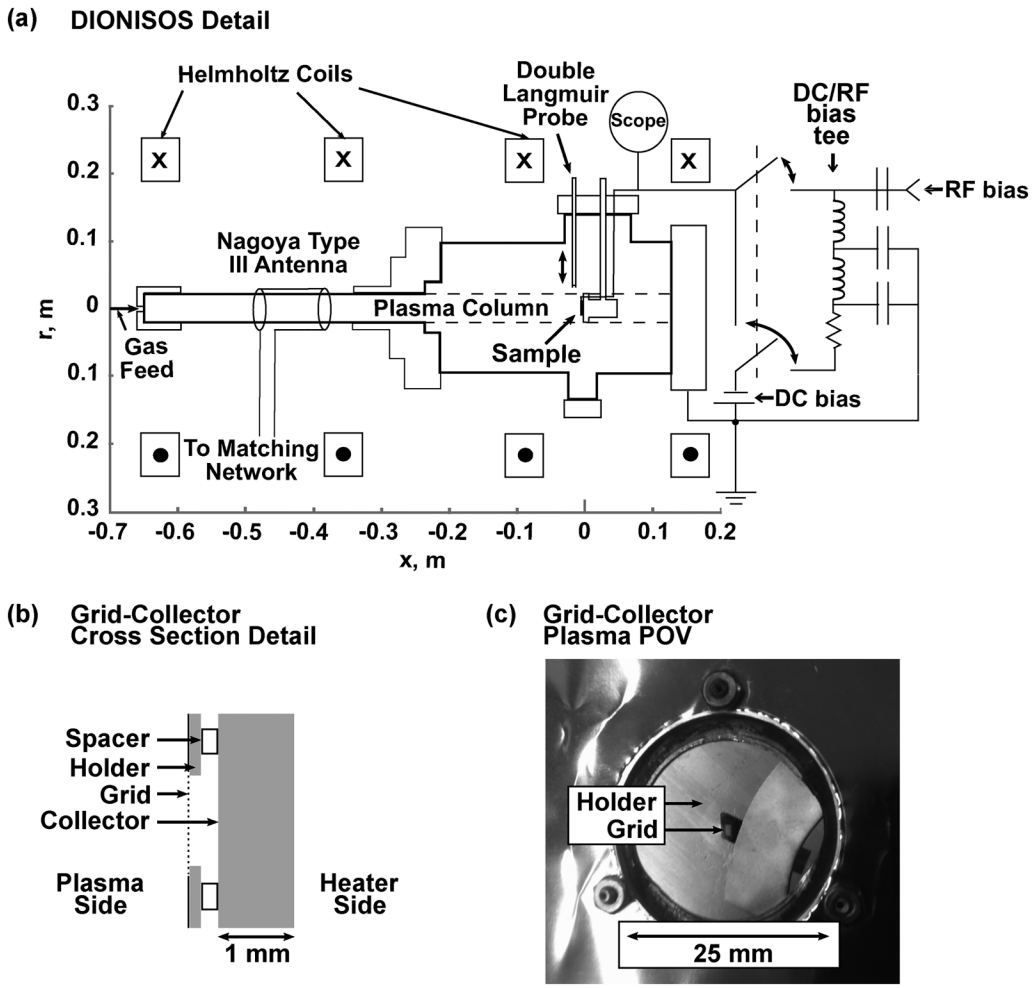

FIG. 2. (a) Schematic of the DIONISOS plasma exposure chamber. The DC/RF biasing circuit is used to bias the sample during plasma exposure or the grid holder during the energy distribution measurements. (b) Profile schematic of the grid-collector retarding field energy analyzer with thicknesses shown to scale. (c), Photo of the surface of the grid-collector energy analyzer from the point of view of the plasma.

supply frequency, 13.56 MHz. The plasma potential is modulated near that frequency, with peak-to-peak potentials of ~40–50 eV on axis. When a DC bias is applied to a W sample, and the plasma density is high enough, the He ions can be extracted from the plasma with modulated energy. The DC bias of the sample was set low enough to avoid sputtering of W by the maximum He ion energy, for which the threshold energy for sputtering is in the range of 100–120 eV. A measurement of the ion energy distribution at r = 0 mm and r = 4 mm in the plasma is displayed in Fig. 3(c).

The plasma flux density was derived from the ion saturation current to a Langmuir probe that could be positioned at different radial locations in the plasma. The flux density radial profiles of the inductively and helicon wave-coupled modes in DIONISOS are displayed in Fig. 3(a). The plasma flux density of the helicon wave-coupled mode of DIONISOS is peaked on axis, as is the plasma potential modulation. Thus, the ion-induced effects are different from the center to the edge along the radius of a single sample. The flux density of He ions at the center of the plasma is twice that of the edge, with a nearly linear dependence between the center and the edge. This would also result in a temperature gradient across the radius of the sample. The effect of the flux density and temperature gradient on the surface morphology is negligible in these flux density and temperature ranges, since the gradient scale length is of the order of tens of millimeters, while diffusion lengths are tens of nanometers at the temperatures used in this experiment. Therefore, the differences in the final surface morphology across the radius of the sample are due to the changes in the ion energy modulation at different flux densities. The temperature gradient is neglected.

The samples are either mounted to a ceramic heater stage for high temperature exposures or to a water-cooled stage for low temperature exposures. The temperature is feedback controlled for the

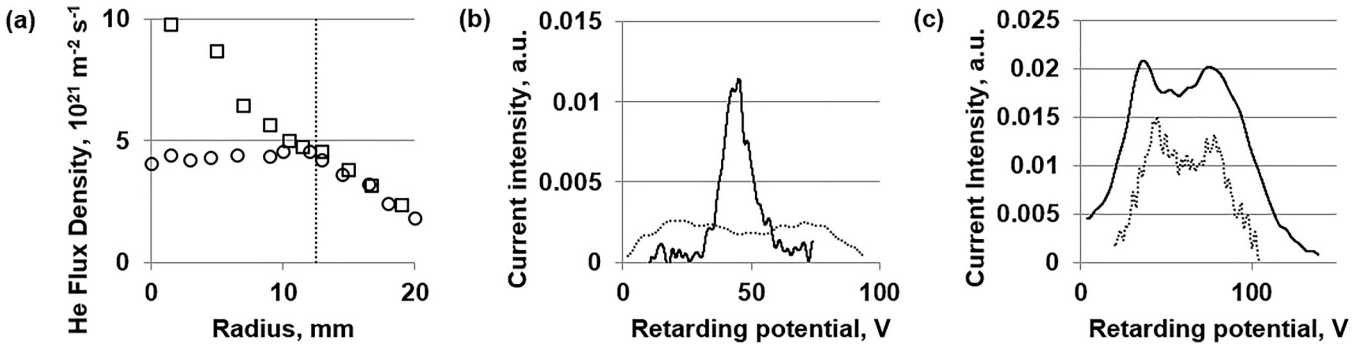

FIG. 3. (a) He ion flux density measured in non-modulating (circles) and modulating (diamonds) plasma modes with respect to radius in the plasma. The radius of the sample is indicated by the vertical dotted line. (b) Ion energy distribution for the non-modulating plasma mode for a DC bias (solid line) and for a DC + RF (dotted line) bias. The DC bias was −50 V for both measurements and the applied RF peak-to-peak bias was 40 V as measured by a high frequency probe attached to the bias feed-through. (c) Ion energy distribution for the intrinsically modulating plasma mode at r = 0 mm (solid line) and r = 4 mm (dotted line). A DC bias of −50 V was applied to the grid for both measurements.

high temperature exposures with a type K thermocouple mounted in the ceramic heater. The surface temperature was monitored with an infrared (IR) pyrometer at a fixed spectral wavelength of 1.6 μm assuming an emissivity of 0.3 for the polished tungsten surfaces. Since the growth of nano-tendrils and fuzz on the surface changes the emissivity, the heater thermocouple was used as a measure of the sample temperature for the high temperature exposures when the surface morphology is expected to change. At the flux densities and ion energies of this work, and with the maximum water cooling capacity of the cooled sample holder, the lowest temperature achieved was 530 K as measured by the IR pyrometer. The low temperature exposures do not have nano-tendril growth, so the pyrometer temperature reading was used to measure the sample temperature in the low temperature exposures.

For Figs. 1(a)–1(c), the polished W sample was exposed with a surface temperature of 1020 K and He flux density of $4.5 \times 10^{21}\,\mathrm{m^{-2}s^{-1}}$ to a He fluence of $5.8 \times 10^{25}\,\mathrm{m^{-2}}$. The time-averaged He ion energy was 48 eV with modulation amplitude of ±22 eV at a frequency of 13.56 MHz. The growth conditions for the layer of fuzz in Fig. 1(d) are identical to Figs. 1(a)–1(c) but with a constant ion energy of 45 eV, i.e., with no applied energy modulation at 13.56 MHz.

C. Orientation imaging measurements

First, fiducial marks were milled into the samples with a focused-ion beam (FIB) using a FEI Helios NanoLab 600 dual beam field emission scanning electron microscope (SEM) with a gallium ion beam. The fiducial marks were used to compare orientation data to images of post-exposure morphology on specific grains. Then, the orientation information was performed on a FEI/Phillips XL30 field emission gun SEM equipped with an EDAX OIM advanced package. A primary electron acceleration voltage of 20 kV was used. The samples were exposed to the modulating plasma mode with ion energy distributions as in Fig. 3(c). After exposure, optical images were taken along the radius of one sample with an AxioCam MRc digital camera attached to a Zeiss ICM 405 optical microscope shown in Fig. 4(a). For greater resolution, electron microscopy was performed on another sample along the radius of the transition region. Full fuzz growth absorbs optical light, so the grains with full fuzz coverage appear darker than grains without full fuzz growth in optical micrographs. In contrast, surfaces with very high curvature emit more secondary electrons than smooth surfaces due to edge effects in electron microscopy, so nano-tendrils and fuzz appear brighter in SEM micrographs than smoother surfaces. For comparing with optical imaging, the color of the SEM images of Fig. 5(b) has been inverted to show full fuzz grains as dark.

We set a threshold gray scale value in the micrographs that corresponded to full fuzz growth grains. We then compared the crystal orientation maps to the micrographs using the fiducial marks milled into the sample before the He exposure for aid in placement and scaling of the images. We cataloged which crystal orientations were associated with the full fuzz (dark) grains on the micrographs and generated inverse pole figures for the five intervals in radius as shown on the radius axis of Figs. 4 and 5. Texture plots were generated for light-only, dark-only, and all grains and were smoothed by harmonic series expansion to the 16th term with a resolution of 5° to help visualize the transition in texture with radius shown in Figs. 4 and 5. The overall grain textures shown in Figs. 4(c) and 5(d) are superpositions of the light and dark grain texture plots just above and below, respectively. The results show that in the far left of the images of Figs. 4(a) and 5(b), or at larger radius, where there are only a few light grains remaining, the texture of these few light grains is close to {101}. The opposite is shown in the far right of the images, which is more toward the center of the samples. In these regions, there are few dark grains, with the texture of the few dark grains close to {001}. It is less straightforward to categorize the other principal orientation {111} since the overall texture, as shown in Figs. 4(c) and 5(d), mainly range between {001} and {101}. However, there is a small sliver toward the {111} orientation shown in the far right texture plot of Fig. 5(e) that indicates that the behavior of the {111} tends to be similar to {001} in this study. This is also observed on individual

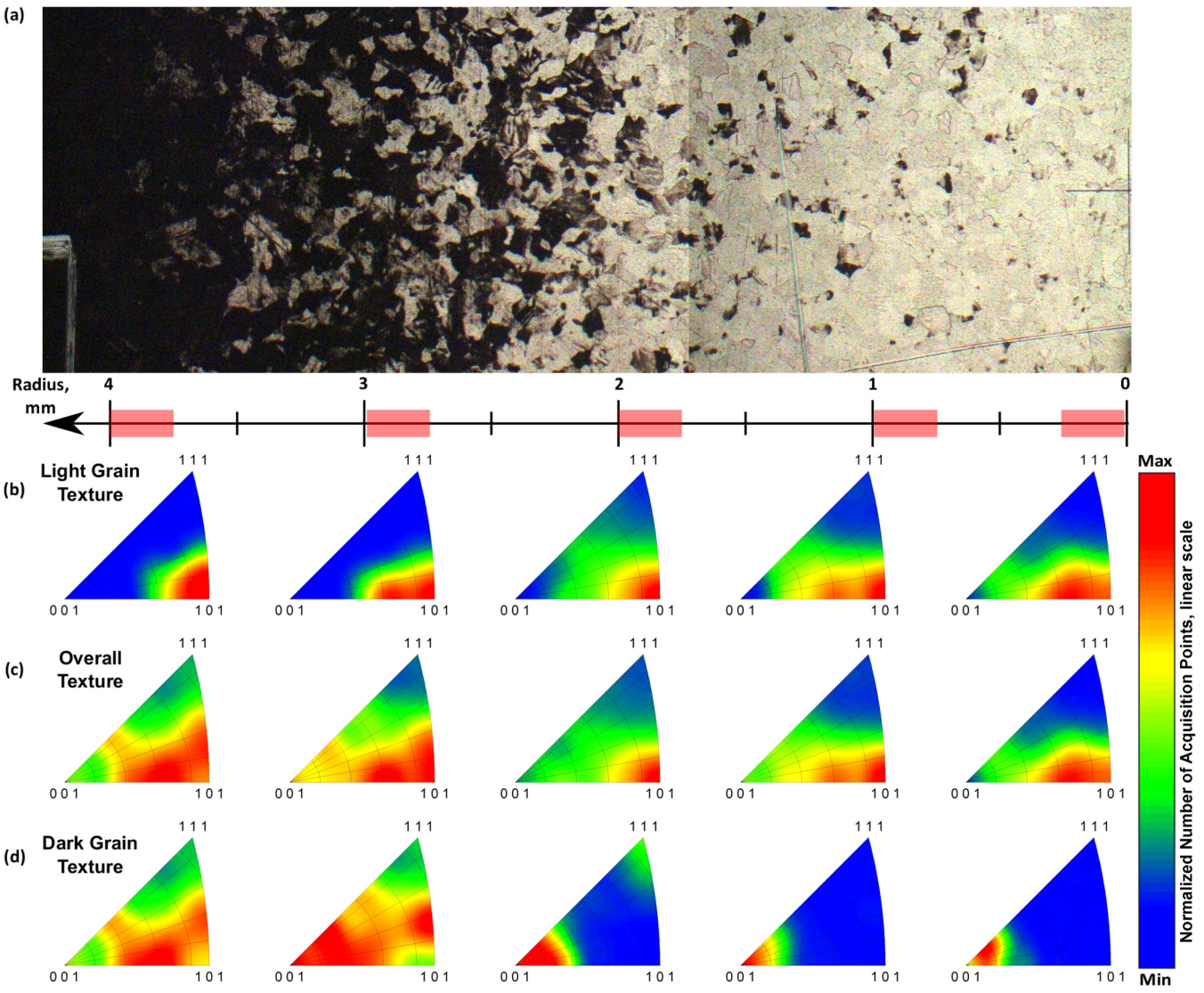

FIG. 4. (a) Composite optical micrograph of the radial transition from full fuzz growth (r > 4 mm, dark surfaces) to varied nanostructure growth (r < 4 mm, mixture of dark and light surfaces). The W sample was heated to 1020 K and subjected to He plasma with peak He ion flux density of 9.7×10^{21} m^{-2} s^{-1} at r = 0 mm and intrinsic ion energy modulation due to the 13.56 MHz RF plasma source for 2500 s. The incident ion properties were as follows: at r = 0 mm, ⟨E⟩ = 55 eV and ΔE = 42 eV; at r = 4 mm, ⟨E⟩ = 60 eV and ΔE = 32 eV. (b) Texture plots of the light grains that have corrugations and isolated nano-tendril/NTB growth. (c) Overall texture plots of all the grains in the corresponding radius interval for comparison to (b) and (d) texture plots. (d) Texture plots of the dark grains that have fuzz growth. The horizontal axis shows red rectangles as the five radial intervals in which the crystal orientation data were used to generate the texture plots of (b), (c), and (d).

grains close in orientation to {111}, which had a high probability of having the uniform W fuzz coverage over the grain.

III. DISCUSSION

A. Nano-tendril bundles

Quasi-uniform W fuzz growth has been reported as a progression from near-surface bubbles, pinholes, and corrugations at low He fluence, with slight variation depending on the crystal orientation,[10,14,33–36] into widespread nano-tendril growth, as long as the sample temperature and He ion energy were above approximately 900 K and 20 eV, respectively. The experimental evidence that has been available so far has shown the inevitable growth of W fuzz over the whole surface of polycrystalline W at long time scales, even despite differences due to grain orientation in pre-fuzz growth. By amplitude modulation of the incident He ion energy, as

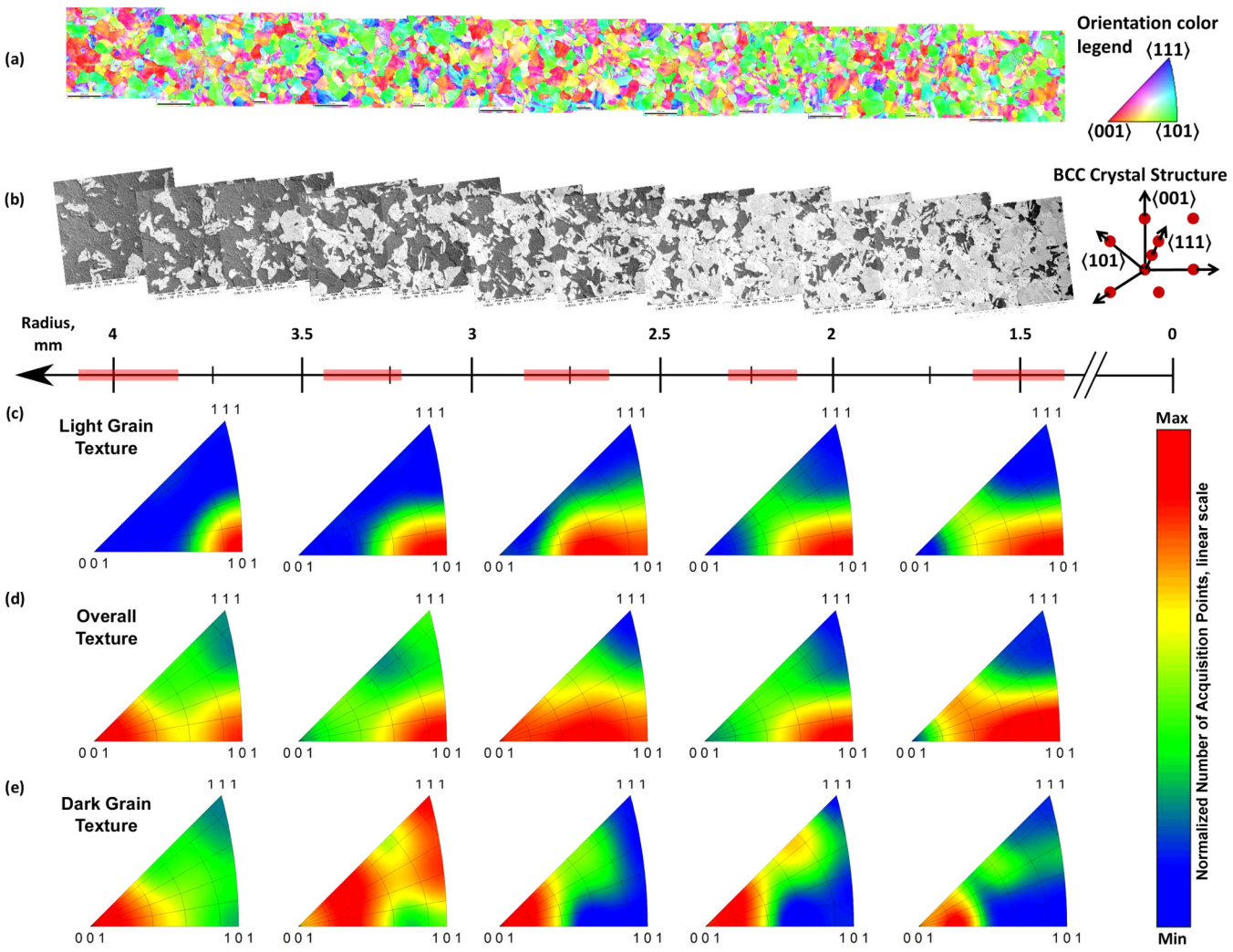

FIG. 5. (a) Composite of OIM orientation maps showing the crystal orientation measured along the radius of the sample before it was exposed to plasma. The inverse pole figure to the right is the color map legend to the stereographic projection of the crystal orientations. (b) Composite of SEM images showing the radial transition from full fuzz growth to varied nanostructure growth. The color of the SEM images has been inverted so that full fuzz growth appears dark and non-full fuzz growth appears light. The W sample was heated and exposed under similar conditions as the sample in Fig. 4. The minimum He fluence was 8.4×10^{24} m^{-2} and occurred at r = 12.7 mm. For r > 4 mm, almost all grains showed full fuzz growth. For r < 1.5 mm, almost all grains had alternative nanostructures of corrugations, nano-tendrils, and NTBs. (c) Texture plots of the grains without full fuzz growth. (d) Texture plots of all the grains to compare to the texture plots of (c) and (e). (e) Texture plots of the grains with full fuzz growth. The horizontal axis for (a) and (b) shows the radial interval in which the crystal orientation data were used to generate the texture plots of (c), (d), and (e) as red rectangles.

opposed to constant ion energy in all previous studies, we have uncovered a rich variety of nanostructures shown in Fig. 1. To demonstrate this, we utilized the plasma mode that results in constant ion energy when a DC bias is applied to the sample. We exposed two W samples to identical He plasmas but with different biasing schemes. One sample had a DC bias, resulting in a constant ion energy of 45 eV, and one had a bias with a DC component equal to the first sample plus an oscillating component at 13.56 MHz, resulting in an ion energy distribution centered around 48 eV but with peaks in the distribution at 26 eV and 70 eV [see Fig. 3(b)]. In the DC case, the sample developed a W fuzz layer over the sample surface with a depth of 0.95 μm after a He fluence of 5.8×10^{25} m^{-2}, as measured by a focused-ion beam (FIB) cross section. The W fuzz layer thickness measured is close to the calculated value of 0.89 μm using the empirically determined one-dimensional growth formula[37] of Baldwin and Doerner with the effective diffusion coefficient for the temperature of 900 K determined by assuming an Arrhenius behavior of the fuzz growth in

this temperature range and including a scaling factor for the lower flux density based on experimental observations at the slightly higher temperature of 1120 K.[38] In contrast, the sample with ion energy modulation showed a wide variety of features including surface corrugation [Fig. 1(a)], isolated nano-tendrils [Fig. 1(b)], and NTB growth [Fig. 1(c)] after exposure to the same background plasma and He ion fluence as the DC case.

The isolated nano-tendrils and NTBs grow much longer away from the surface than the fuzz growth in the DC case yet clearly are constituted of nano-tendrils like those in fuzz, providing valuable insight into the tendril growth mechanisms. These isolated structures, existing at spatial scales much smaller than grain sizes, indicate that the ion energy modulation effectively increases the growth rate of nano-tendrils.

Further insights on tendril growth are obtained by imaging the surface below and adjacent to an NTB structure. Under plasma exposure conditions with modulated He ion energy as above, with He ion flux density of $1.6 \times 10^{22}\,m^{-2}\,s^{-1}$ and surface temperature of 1020 K, large NTBs were observed after a He ion fluence of $7.6 \times 10^{25}\,m^{-2}$. One such NTB was coated in platinum (Pt), cross-sectioned by FIB milling, and imaged with the SEM (Fig. 6). Cavities from blistering of W after deuterium plasma exposure has been shown to be prevalent in the first 5 μm near the surface.[39] Just below the surface of the NTB and down to 5 μm deep into the bulk, there is no evidence of voids, or a depression in the bulk W, that would have supplied the W that formed the NTB [see Fig. 6(b)]; in fact, quite the opposite, the W in the NTB certainly originates from the surrounding surface. A high-resolution image analysis of the dotted rectangle area of Fig. 6(b) shown in Fig. 6(c) shows the NTB situated on top of a small "pedestal" of solid W that is 150 nm higher than the smooth surface around the NTB. The quantity of W atoms in the NTB tendrils is the equivalent of a solid W disk with 150 nm thickness and ~35 micrometer radius; a distance approximately half of the lateral spacing between NTBs on the surface. The most robust interpretation is that the "pedestal" is actually at the original height of the W surface, and the surrounding surface has been lowered by providing W atoms to the NTB. Furthermore, the NTB is clearly attached to the surface, as we observe the nano-tendrils extend from the bulk surface into the NTB. Thus, surface migration of W could form the NTB.

Conversely, it is not possible that the migration is due to the W atoms becoming free of the surface due to some erosion mechanism and re-depositing in the NTB. First, the majority of incident He ions have energies below the threshold for physical sputtering, which is ~110 eV for He incident on W.[40] Impurities would sputter at lower energy, but impurities in the chamber or plasma have been searched for with a residual gas analyzer and an optical emission spectrometer, respectively, with negligible impurity levels observed. Second, if there was a flux of W atoms away from the surface surrounding the NTB/nano-tendrils by some unspecified erosion mechanism, simple geometry arguments disallow the NTB/nano-tendrils to grow from line of sight accumulation of the eroded W, due to the vanishingly small solid angle subtended by the NTB to surrounding surfaces. Thus, the only conclusion is that the tendrils must be formed by rapid surface migration of the W to the NTB/nano-tendril structures, presumably by W adatoms. This is feasible from an energy point of view because the production of adatoms by ion bombardment will have a lower energy threshold than sputtering.[41] Given the compelling visual evidence for the adatom migration mode of tendril growth, we now examine other features of the growth conditions both for general validation of the model and insight as to why ion energy modulation produces these isolated nano-tendril structures.

B. Crystal orientation and ion energy modulation dependence

Helium plasma with a peak He ion flux density of $9.7 \times 10^{21}\,m^{-2}s^{-1}$ and with plasma potential modulation as a function of radius in the cylindrical plasma was used to irradiate a W sample at 1020 K. In this case, the ion energy modulation was intrinsically produced in the plasma by the RF helicon wave mode coupling, not by external bias modulation. The energy distribution was directly measured with a gridded ion energy analyzer. At the center of the sample, the average ion energy was 55 eV with an amplitude modulation of 42 eV peak-to-peak at 13.56 MHz. The peak-to-peak amplitude decreases with increasing plasma radius, so that at r = 4 mm, the peak-to-peak amplitude is 32 eV, while the average ion energy increases slightly to 60 eV. After 2500 s of exposure, the variation in ion energy modulation with radius resulted in grain-to-grain variation in nanostructure growth along the radius of the sample (see Fig. 4). Under these conditions, the sample remained macroscopically reflective, with the majority of the grains absent of W fuzz growth. However, this region does possess corrugations and isolated nano-tendril/NTB structures (not visible in Fig. 4). This is broadly consistent with the results of the external ion energy modulation demonstration experiment of Fig. 1. At larger radii, the energy amplitude modulation and flux density decrease, but the surface temperature is approximately unchanged. As seen in Fig. 4, lower ion energy amplitude modulation and flux density resulted in 100% fuzz growth coverage, similar to the constant ion energy case of Fig. 1(d).

The transition region (0 mm < r < 4 mm) shows grains that have full fuzz growth coverage immediately adjacent to other grains that instead have nano-tendril/NTB structures (Fig. 4). Full fuzz growth absorbs light, so the grains with full fuzz coverage appear black in the optical images of Figs. 4(a) and 7(a). Starting at larger radii (i.e., r > 4 mm at left of the image in Fig. 4), every grain shows full fuzz growth. Moving to the right in the image, the grains that first exhibit NTB growth and retain macroscopic optical reflectivity have a {101} texture [see Fig. 4(b)]. It should be noted that the overall grain texture of the sample is not uniform, as shown in Fig. 3(c), but mainly has {101} and {001} components, with the {111} type grains contributing less than 5% to the overall texture. The {001} type grains are the only type to show full fuzz growth [see Figs. 4(d) and 5(e)] near the center of the sample (r < 0.5 mm) where the ion energy amplitude modulation and flux density are the greatest. The conclusion of Figs. 4 and 5 is that under conditions of 13.56 MHz ion energy modulation, the dominant tendril growth structure (i.e., fuzz or NTB) is highly dependent on individual grain orientation.

The change in He fluence (or flux) across the sample is not the cause of the radial variation in fuzz growth. This is first obvious by the variation in tendril growth on adjacent grains that have

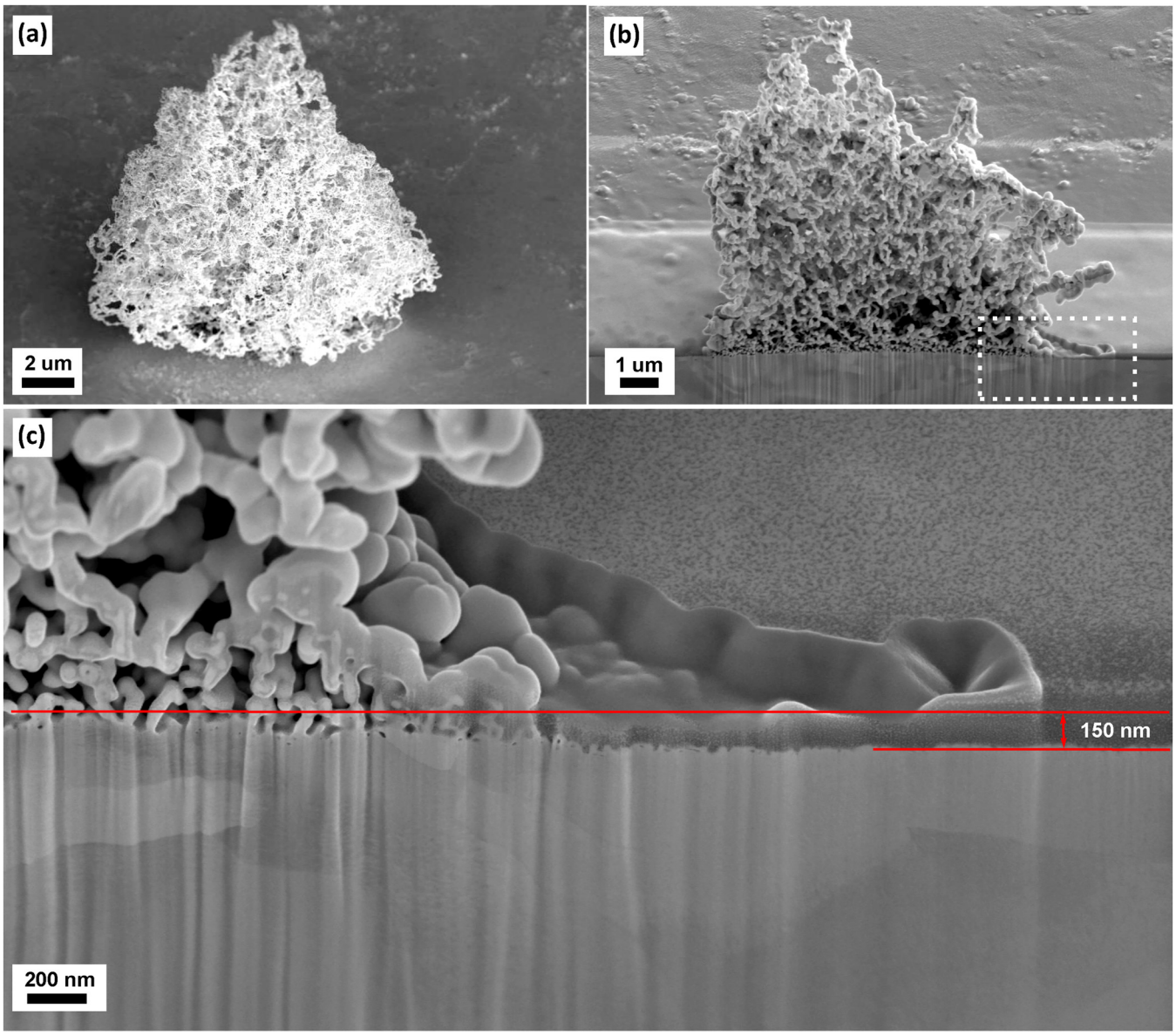

FIG. 6. (a) Image of a NTB that developed due to ion energy modulation in a He plasma with a He flux density of $1.6 \times 10^{22}\,m^{-2}s^{-1}$ after a He fluence of $7.6 \times 10^{25}\,m^{-2}$. The surface temperature was 1020 K. (b) Cross section by FIB milling of the NTB in (a). (c) High-resolution image of area shown by the dotted rectangle in (b). The height of the NTB in this cross section is 10 μm and the diameter of the individual nano-tendrils within the NTB range from 40 to 100 nm.

effectively identical fluence. Second, others have shown that at low He fluence, precursor structures such as corrugations[10,33–35] and loops[14] are observed rather than fuzz. The fluence necessary prior to fuzz growth has been called an incubation fluence,[38,42,43] and its value is reported in the range $1.5–4 \times 10^{24}\,m^{-2}$ in the temperature range of 1000–1200 K. In Fig. 4, the lowest He fluence on the sample is $8.4 \times 10^{24}\,m^{-2}$—well in excess of the incubation fluence. Also, full fuzz growth occurred on the sample in Fig. 4 for *lower* flux density/fluence regions (larger radii). If the ion irradiation was monoenergetic, the fuzz growth would increase with the flux density/fluence, which is the opposite of what is observed here.

Since ion energy modulation has been shown here to inhibit fuzz growth on an initially smooth surface, we decided to test the effect of ion energy modulation on a sample with full fuzz already grown on the surface. Tungsten fuzz was grown on two samples with the same exposure conditions. One sample was used for

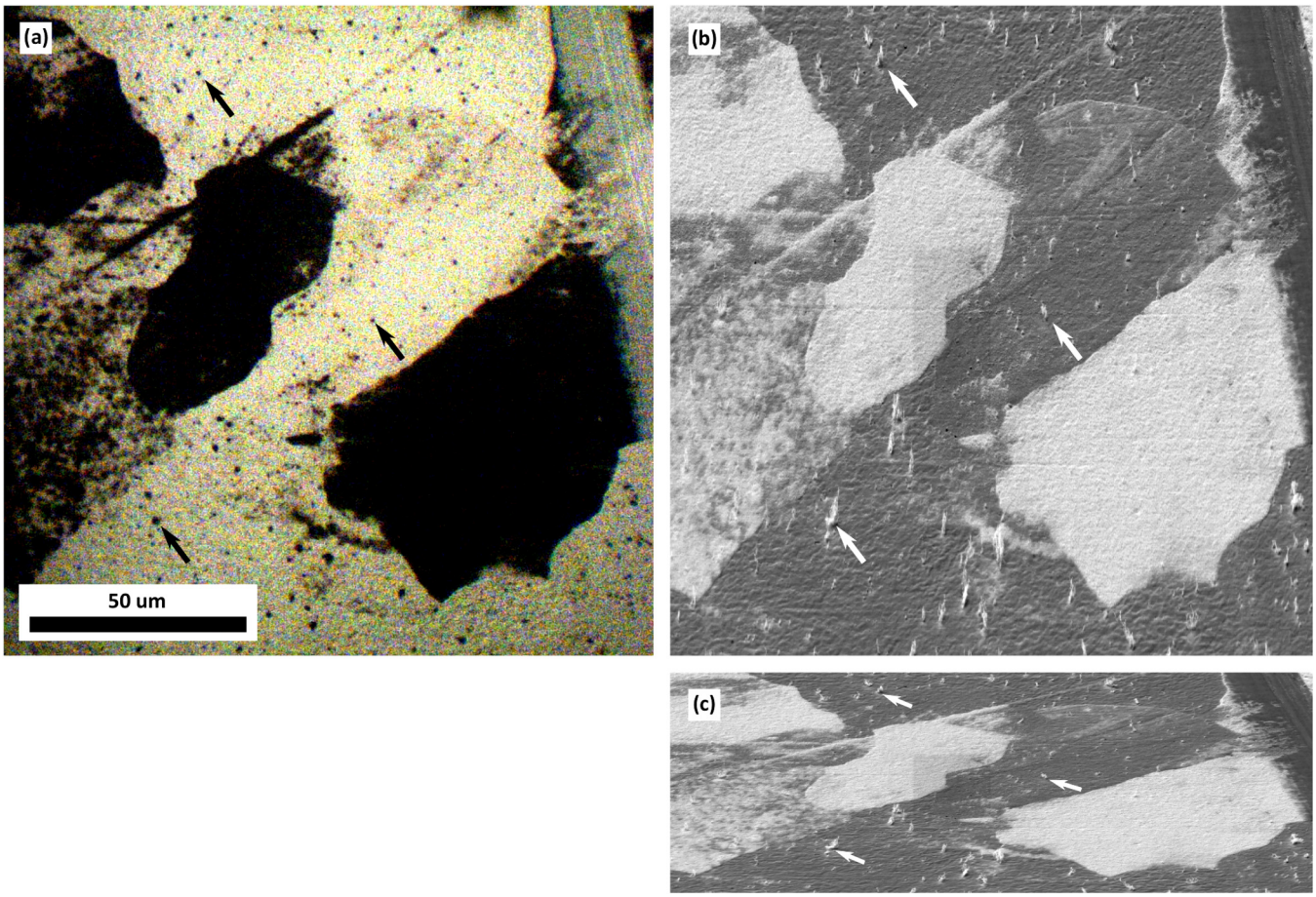

FIG. 7. (a) Higher magnification optical micrograph at r = 2 mm from the sample in Fig. 4 viewing perpendicular to the surface. The black areas are grains with fuzz growth and the small black dots are isolated nano-tendrils (NTBs). The arrows highlight three corresponding NTBs among the images, but there are over 100 NTBs in the viewed area. (b) SEM micrograph of the same area as (a). The sample was tilted by 70° from the electron beam in the SEM for orientation analysis. The *y* direction in the electron micrograph is corrected so that the surface plane appears normal to the viewing direction, like in (a). The fuzz and NTBs are brighter than the smoother surface because high curvature surfaces emit more electrons due to edge effects. (c) Same electron micrograph as (b) without the *y* direction corrected for tilt, showing the view along the electron beam direction and the large NTBs. The scale bar in (a) is valid for (b) and (c), as well as for the horizontal direction.

imaging the fuzz [Fig. 8(a)], and the second sample was imaged after exposure to the helicon wave-coupled plasma with ion energy modulation of $\Delta E = 42$ eV [Fig. 8(b)]. After being subjected to the He ion energy modulation, the surface regained macroscopic reflectivity and, upon microscopic inspection, exhibited clear NTB growth [Fig. 8(c)]. The surface regained macroscopic reflectivity because the surface roughness decreased during the exposure to the plasma with ion energy modulation. This test verifies that ion energy modulation produces surface W migration conditions that both promote NTBs and alter existing nano-tendrils. Importantly, this reconfirms that surface mobility is commonly governing the creation/destruction of tendrils in NTBs/fuzz. The coverage of NTBs is greater when the initial surface condition is W fuzz vs smooth, but this may simply be due to the greater roughness W fuzz promoting a higher probability of NTB growth. Tungsten fuzz surfaces can be made smooth again by high temperature (>1000 K) annealing.[44] In this case, ion energy modulation may be inhibiting nano-tendril growth in specific locations and the high temperature is activating nano-tendril decomposition by surface tension forces.

There is an obvious large impact of both grain orientation and ion energy modulation involved in determining the dominant type of nanostructure produced on a grain. A heuristic explanation based on adatom surface migration follows; tendril growth is set by the time-dependent rate competition between production, annihilation with vacancies (produced simultaneously with adatoms during ion bombardment), diffusion, and incorporation into nano-tendrils. While a detailed model is beyond the scope of this paper, we can examine how the trends of our new experimental observations follow this explanation.

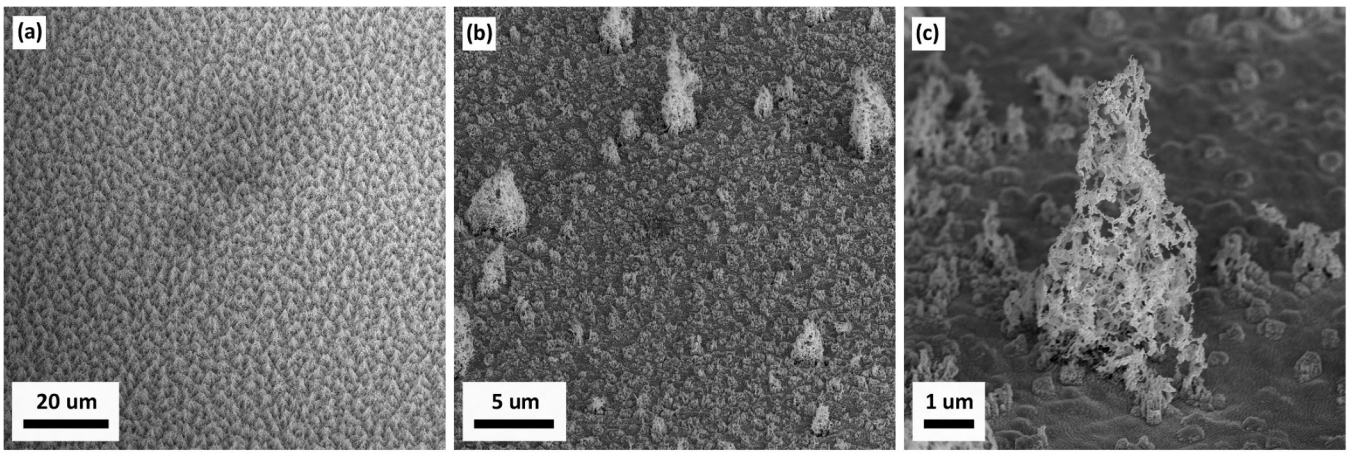

FIG. 8. (a) SEM image of a W sample at 1020 K exposed to a He flux density of 2.6×10^{21} m^{-2} s^{-1} with a DC bias of −50 V for 3000 s, resulting in W fuzz. (b) SEM image of a W sample prepared in the same way as in (a) and then exposed at 1020 K to a He ion flux density of 9.7×10^{21} m^{-2} s^{-1} with intrinsic He ion energy modulation at 13.56 MHz for 5000 s. The average ion energy and peak-to-peak ion energy were $\langle E \rangle = 55$ eV and $\Delta E = 42$ eV, respectively. (c) Higher magnification image of a NTB and the surface detail on the sample in (a). The viewing angle for each micrograph is 52°.

1. Adatoms are produced predominantly by He ion bombardment, since the thermal equilibrium adatom concentration at these temperatures is negligibly low. The yield of adatoms per incident ion is a nonlinear function of the incident ion energy above the threshold for adatom production.[19,41,45] This adatom production rate is varied instantaneously by the energy modulation present. Also, the adatom yield is dependent on the surface crystal orientation. Surface orientations with higher roughness have lower surface binding energy[46] and so would yield more adatoms per ion of a given energy. Thus, the adatom production rate is granular and temporally dependent.
2. The isolated nano-tendril/NTB growth favors a situation where the energy modulation is largest. In this case, the instantaneous rate of adatom production will be both the highest and the lowest at the zenith (55 eV + 21 eV = 76 eV) and nadir (55 eV − 21 eV = 34 eV), respectively, of the modulation period in Fig. 3. This could present a change in adatom yield by up to an order of magnitude over the period of the modulation (74 ns for $f_{RF} = 13.56$ MHz).
3. The change in the adatom production rate over the period of the energy modulation impacts the rate competition between kinetic and thermal effects sufficiently to modify the nano-tendril nucleation on the surface, i.e., the ion energy modulation is effectively decreasing the lifetime of nano-tendrils, or characteristic time for nano-tendril decay. This decreases the quasi-steady state coverage of nano-tendrils. With fewer nano-tendrils, their growth rate increases, ultimately limited by the diffusivity of the adatoms.
4. The hierarchy of surface self-diffusivity of W,[47,48] i.e., W adatom migration on a W substrate, is such that the {101} plane has higher diffusivity than the {111} and {001} planes. This is because the {101} plane is the close-packed plane of the body centered cubic crystal structure of W. Under the same ion energy modulation and fluence, isolated structures occur on grains with higher diffusivity. This is consistent with the requirement that the isolated nano-tendril/NTB must form from larger average migration distances than occurs with uniform fuzz. Conversely, uniform fuzz favors slower diffusion.

IV. SUMMARY

We have shown that the surface diffusion of loosely attached atoms (adatoms) plays a significant role in the growth of nano-tendril structures on tungsten subjected to low-energy helium ion bombardment. The disparity in growth under ion energy modulation conditions shows that distinct growth modes dominate on different grains depending on the crystal orientation of the grain. This shows that the final surface structures can be manipulated in RF plasma and could be applied to other metals or semiconductors to study surface diffusion barriers of material surfaces or tailor surface morphology.

AUTHORS' CONTRIBUTIONS

K.B.W. performed the experiments and characterized the materials and wrote the original manuscript. D.G.W. provided resources, supervision, and administration for the study. G.M.W. supervised the experiments. All authors reviewed and edited the manuscript.

ACKNOWLEDGMENTS

This work was supported by the U.S. DOE (Award Nos. DE-SC00-02060 and DE-FC02-99ER54512). This work made use of the MRSEC Shared Experimental Facilities at MIT, supported by the National Science Foundation under Award No. DMR-08-19762.

DATA AVAILABILITY

The data that support the findings of this study are available from the corresponding author upon reasonable request.

REFERENCES

[1]R. A. Pitts, S. Carpentier, F. Escourbiac, T. Hirai, V. Komarov, S. Lisgo, A. S. Kukushkin, A. Loarte, M. Merola, A. Sashala Naik, R. Mitteau, M. Sugihara, B. Bazylev, and P. C. Stangeby, J. Nucl. Mater. **438**, S48 (2013).
[2]G. De Temmerman, T. Hirai, and R. A. Pitts, Plasma Phys. Control. Fusion **60**, 044018 (2018).
[3]S. Kajita, S. Takamura, N. Ohno, D. Nishijima, H. Iwakiri, and N. Yoshida, Nucl. Fusion **47**, 1358 (2007).
[4]M. de Respinis, G. De Temmerman, I. Tanyeli, M. C. M. van de Sanden, R. P. Doerner, M. J. Baldwin, and R. van de Krol, ACS Appl. Mater. Interfaces **5**, 7621 (2013).
[5]S. Kajita, T. Yoshida, D. Kitaoka, R. Etoh, M. Yajima, N. Ohno, H. Yoshida, N. Yoshida, and Y. Terao, J. Appl. Phys. **113**, 134301 (2013).
[6]İ Tanyeli, L. Marot, D. Mathys, M. C. M. van de Sanden, and G. De Temmerman, Sci. Rep. **5**, 9779 (2015).
[7]D. Hwangbo, S. Kawaguchi, S. Kajita, and N. Ohno, Nucl. Mater. Energy **12**, 386 (2017).
[8]H. Iwakiri, K. Yasunaga, K. Morishita, and N. Yoshida, J. Nucl. Mater. **283–287**, 1134 (2000).
[9]H. Trinkaus, J. Nucl. Mater. **133–134**, 105 (1985).
[10]P. Fiflis, D. Curreli, and D. N. Ruzic, Nucl. Fusion **55**, 33020 (2015).
[11]R. D. Smirnov, S. I. Krasheninnikov, and J. Guterl, J. Nucl. Mater. **463**, 359 (2015).
[12]A. M. Ito, A. Takayama, Y. Oda, T. Tamura, R. Kobayashi, T. Hattori, S. Ogata, N. Ohno, S. Kajita, M. Yajima, Y. Noiri, Y. Yoshimoto, S. Saito, S. Takamura, T. Murashima, M. Miyamoto, and H. Nakamura, Nucl. Fusion **55**, 073013 (2015).
[13]L. Sandoval, D. Perez, B. P. Uberuaga, and A. F. Voter, Phys. Rev. Lett. **114**, 105502 (2015).
[14]S. Takamura and Y. Uesugi, Appl. Surf. Sci. **356**, 888 (2015).
[15]A. Lasa, S. K. Tähtinen, and K. Nordlund, EPL **105**, 25002 (2014).
[16]S. Kajita, N. Yoshida, N. Ohno, and Y. Tsuji, New J. Phys. **17**, 1 (2015).
[17]H. Fan, Y. Zhang, D. Liu, C. Niu, L. Liu, W. Ni, Y. Xia, Z. Bi, Y. Hong, G. Benstetter, and G. Lei, Nucl. Fusion **60**, 046011 (2020).
[18]S. I. Krasheninnikov, Phys. Scr. **T145**, 014040 (2011).
[19]Y. V. Martynenko and M. Y. Nagel, Plasma Phys. Rep. **38**, 996 (2012).
[20]D. Trufanov, E. Marenkov, and S. Krasheninnikov, Phys. Procedia **71**, 20 (2015).
[21]K. B. Woller, D. G. Whyte, and G. M. Wright, J. Nucl. Mater. **463**, 289 (2015).
[22]K. B. Woller, D. G. Whyte, G. M. Wright, R. P. Doerner, and G. De Temmerman, J. Nucl. Mater. **438**, S913 (2013).
[23]K. B. Woller, D. G. Whyte, and G. M. Wright, Nucl. Mater. Energy **12**, 1282 (2017).
[24]K. B. Woller, D. G. Whyte, and G. M. Wright, Nucl. Fusion **57**, 066005 (2017).
[25]S. Kajita, S. Kawaguchi, N. Yoshida, N. Ohno, and H. Tanaka, Nucl. Fusion **58**, 106002 (2018).
[26]D. Hwangbo, S. Kajita, N. Ohno, P. McCarthy, J. W. Bradley, and H. Tanaka, Nucl. Fusion **58**, 096022 (2018).
[27]S. Takamura, Y. Uesugi, A. M. Ito, M. Yajima, K. Yamada, S. Maenaka, and K. Fujita, Nucl. Fusion **57**, 086043 (2017).
[28]G. M. Wright, H. S. Barnard, L. A. Kesler, E. E. Peterson, P. W. Stahle, R. M. Sullivan, D. G. Whyte, and K. B. Woller, Rev. Sci. Instrum. **85**, 023503 (2014).
[29]K. B. Woller, D. G. Whyte, and G. M. Wright, Phys. Plasmas **24**, 053513 (2017).
[30]K. B. Woller, D. G. Whyte, G. M. Wright, and D. Brunner, J. Nucl. Mater. **481**, 111 (2016).
[31]D. Brunner, B. LaBombard, R. Ochoukov, and D. Whyte, Rev. Sci. Instrum. **84**, 033502 (2013).
[32]R. A. Pitts, Contrib. Plasma Phys. **36**, 87 (1996).
[33]N. Ohno, Y. Hirahata, M. Yamagiwa, S. Kajita, M. Takagi, N. Yoshida, R. Yoshihara, T. Tokunaga, and M. Tokitani, J. Nucl. Mater. **438**, S879 (2013).
[34]C. M. Parish, H. Hijazi, H. M. Meyer, and F. W. Meyer, Acta Mater. **62**, 173 (2014).
[35]S. Kajita, N. Yoshida, N. Ohno, Y. Hirahata, and R. Yoshihara, Phys. Scr. **89**, 025602 (2014).
[36]A. Khan, G. De Temmerman, T. W. Morgan, and M. B. Ward, J. Nucl. Mater. **474**, 99 (2016).
[37]M. J. Baldwin and R. P. Doerner, Nucl. Fusion **48**, 035001 (2008).
[38]M. J. Baldwin, R. P. Doerner, D. Nishijima, K. Tokunaga, and Y. Ueda, J. Nucl. Mater. **390–391**, 886 (2009).
[39]M. H. J. 't Hoen, M. Balden, A. Manhard, M. Mayer, S. Elgeti, A. W. Kleyn, and P. A. Zeijlmans van Emmichoven, Nucl. Fusion **54**, 083014 (2014).
[40]W. Eckstein, *Calculated Sputtering, Reflection and Range Values* (Garching, 2002).
[41]R. P. Doerner, S. I. Krasheninnikov, and K. Schmid, J. Appl. Phys. **95**, 4471 (2004).
[42]S. Kajita, T. Yokochi, N. Ohno, and T. Kumano, Jpn. J. Appl. Phys. **51**, 01AJ03 (2012).
[43]T. J. Petty, M. J. Baldwin, M. I. Hasan, R. P. Doerner, and J. W. Bradley, Nucl. Fusion **55**, 093033 (2015).
[44]G. M. Wright, G. G. Van Eden, L. A. Kesler, G. De Temmerman, D. G. Whyte, and K. B. Woller, J. Nucl. Mater. **463**, 294 (2015).
[45]H. Gades and H. M. Urbassek, Phys. Rev. B **50**, 11167 (1994).
[46]P. Wynblatt and N. A. Gjostein, Surf. Sci. **22**, 125 (1970).
[47]W. R. Graham and G. Ehrlich, Thin Solid Films **25**, 85 (1975).
[48]G. L. Kellogg, Surf. Sci. Rep. **21**, 1 (1994).